



ORIGINAL ARTICLE

High temperature compressive creep behavior of $\text{BaCe}_{0.65}\text{Zr}_{0.2}\text{Y}_{0.15}\text{O}_{3-\delta}$ in air and 4% H_2/Ar Wenyu Zhou^{1,2}  | Jürgen Malzbender¹ | Wendelin Deibert¹ | Olivier Guillon¹  | Ruth Schwaiger^{1,3} | Arian Nijmeijer² | Wilhelm Albert Meulenbergh^{1,2}¹Institute of Energy and Climate Research (IEK), Forschungszentrum Jülich GmbH, Jülich, Germany²Faculty of Science and Technology, Inorganic Membranes, University of Twente, Enschede, The Netherlands³Chair of Energy Engineering Materials, RWTH Aachen University, Aachen, Germany

Correspondence

Wenyu Zhou, Forschungszentrum Jülich GmbH, Institute of Energy and Climate Research (IEK), 52425 Jülich, Germany. Email: w.zhou@fz-juelich.de

Funding information

China Scholarship Council (CSC)

Abstract

The proton conductive material $\text{BaCe}_{0.65}\text{Zr}_{0.2}\text{Y}_{0.15}\text{O}_{3-\delta}$ has great potential for the separation and purification of hydrogen. However, due to the demanding application conditions regarding both temperature and atmosphere, the elevated temperature structural stability needs to be characterized and warranted. Hence, in this research work, the elevated temperature compressive creep behavior of $\text{BaCe}_{0.65}\text{Zr}_{0.2}\text{Y}_{0.15}\text{O}_{3-\delta}$ in the temperature regime of 850°C to 1200°C was studied in both air and 4% H_2/Ar as a function of the applied stress. The results indicate different creep mechanisms depending on atmosphere and temperature range. While dislocation creep was observed in 4% H_2/Ar over the full range, a dislocation creep mechanism was observed in air at temperatures $\leq 1050^\circ\text{C}$ and a diffusional creep mechanism at temperature $\geq 1100^\circ\text{C}$. A detailed microstructural analysis of the post-creep test specimens revealed that the exposure to oxygen leads to localized stoichiometric changes and a decomposition at the surface.

KEYWORDS

 $\text{BaCe}_{0.65}\text{Zr}_{0.2}\text{Y}_{0.15}\text{O}_{3-\delta}$, creep, mechanical properties, microstructure, proton conductor

1 | INTRODUCTION

BaCeO_3 -based materials have raised considerable interest due to their high protonic conductivity.^{1–7} In particular, when Zr is partially substituted into the parent material BaCeO_3 , enhanced chemical resistances against H_2O , CO_2 and H_2S are observed.^{8–14} Hence, $\text{BaCe}_{0.65}\text{Zr}_{0.2}\text{Y}_{0.15}\text{O}_{3-\delta}$ (BCZ20Y15) verified both good protonic conductivity and chemical stability^{8,14–16} and is therefore considered to be a promising material for hydrogen separation applications. BCZ20Y15, when combined with Gd-doped CeO_2 , forms a dual-phase proton conductive membrane with a remarkably high H_2 permeance.¹⁴

Under application relevant conditions, these proton conducting membranes are operated at an intermediate

temperature ($\sim 600^\circ\text{C}$ – 800°C) and are potentially exposed to high pressure differences across the membrane.^{14,17} Under such harsh conditions, the membrane must maintain its structural and geometrical stability, ideally over an operation period of many years, which means that the mechanical stability is a matter of concern.

During operation of these membranes, stresses acting on the membrane components,^{17,18} combined with the elevated temperature, potentially lead to the occurrence of creep. Creep becomes noticeable for ceramics typically when the temperature is higher than around half of the melting temperature.¹⁹ From an engineering point of view, the membrane material should not creep more than 1% per year in a compressive creep mode (corresponding to $\sim 3 \times 10^{-10}/\text{s}$) to warrant reliable long-term operation.²⁰ Creep behavior of

This is an open access article under the terms of the Creative Commons Attribution-NonCommercial-NoDerivs License, which permits use and distribution in any medium, provided the original work is properly cited, the use is non-commercial and no modifications or adaptations are made.

© 2021 The Authors. *Journal of the American Ceramic Society* published by Wiley Periodicals LLC on behalf of American Ceramic Society (ACERS).

the material at elevated temperature under constant loads can be used to demonstrate the material's thermomechanical reliability and creep resistance,²¹⁻²⁴ which can potentially guide membrane component design.

The aim of this work was to characterize the creep behavior of BCZ20Y15 at elevated temperatures from 850°C to 1200°C, in both air and 4% H₂/Ar. Based on the observed creep behaviors, a detailed investigation of the creep mechanisms was carried out. Based on post-creep microstructure investigation, the main factors that are critical to the mechanical and operational stability are discussed.

2 | EXPERIMENTAL PROCEDURE

BCZ20Y15 samples were prepared by a solid-state reaction method (SSR). BaCO₃ (99%, Sigma Aldrich), CeO₂ (99.9%, Sigma Aldrich), ZrO₂ (99%, Sigma Aldrich), and Y₂O₃ (99%, Sigma Aldrich) were used as starting materials. In the process, precursor powders were mixed in stoichiometric ratios and ball-milled in ethanol for 24 h. The resultant mixtures were dried at 80°C and then calcined at 1300°C for 5 h in air. 0.5 wt% NiO (99%, Sigma Aldrich)¹⁴ was added as sintering aid after pre-calcination in order to obtain dense samples. To obtain powders with a fine and homogeneous grain size, calcined BCZ20Y15 powders were ball-milled (ZrO₂ balls, 3.5 mm diameter, weight ratio powder: balls: ethanol = 1: 2: 3) in ethanol for 24 h. Afterwards, the mixtures were dried and sieved through a 160 µm mesh.

Bar-shaped samples were then uniaxially pressed under a pressure of ~20 MPa for 5 min to obtain a green density of ~60%, with a specimen geometry of ~5 × 5 × 40 mm³. The samples were subsequently sintered at 1500°C for 5 h in air at constant heating / cooling rates of 5 K min⁻¹.

Detailed information regarding the material preparation, crystal structure, and phase purity of the sintered samples can be found in Ref. [25].

The microstructures were assessed by a Zeiss SUPRA 50VP field emission scanning electron microscope (SEM, Zeiss Microscopy GmbH). Prior to the microstructural analysis, the specimen was embedded in epoxy resin, ground sequentially using SiO₂ sandpaper with 400 and 2000 grit size and then polished using 6 and 1 µm diamond suspensions. The final polishing was conducted using 50 nm colloidal silica polishing suspension. The image analysis software Image J²⁶ was used to determine the grain size and porosity from the SEM images. Energy dispersive X-ray (EDX) spectroscopy was carried out at 10 kV accelerating voltage using a X-Max 80 detector and the AZtec data acquisition and analysis software package (Oxford Instruments Nanoanalysis, High Wycombe, United Kingdom).

For creep testing, BCZ20Y15 samples were cut by an electrical discharge machine into specimens with the dimension of ~4 × 4 × 10 mm³. Similar as reported in Ref. [27-30], the steady-state creep rates were obtained by the application of long-term compressive tests at different temperatures and applied stresses. The details of the setup used for creep testing can be found in Ref. [27,29,30]. The creep tests in 4% H₂/Ar were carried out in the temperature range from 850°C to 1000°C (maximum temperature limited by the experimental setup) and in air from 1000°C to 1200°C under uniaxial compressive loads. The chosen test temperatures were higher than the material application temperature for a reliably creep behavior observation. A further extrapolation based on Arrhenius plot can help to estimate the creep condition of the material in the application temperature. The temperature was increased at a rate of 8 K/min, and kept constant after reaching the test temperature for two hours in order to allow the specimen to reach thermal equilibrium. A preload of ~2 N was applied during heating and thermal equilibrium to keep the specimen fixed in position. Stresses ranging from 30 to 80 MPa were applied to determine the creep rates. A maximum applied stress of ~95 MPa, at which the specimens fractured, had been determined beforehand. The minimum applied stress was fixed according to simulation results reported in literature³¹ indicating that 30 MPa will likely occur under realistic gas separation operation conditions. The creep analysis was carried out on the basis of data that confirmed steady-state deformation and continued until the integral deformation reached ~100 µm or until a maximum test duration of 24 h was reached.

For the tests in 4% H₂/Ar, the chamber was firstly purged at room temperature with the gas until the oxygen partial pressure in the chamber was lower than 1 mbar (several hundred ppm oxygen content). During heating to the test temperature, the remaining oxygen in the chamber reacted with the H₂ resulting in ~0 ppm O₂ content at the test temperature. For the tests in air, the oxygen partial pressure was ~0.2 bar, which is distinctly different compared to the condition in the 4% H₂/Ar tests.

Every specimen was examined in subsequent steps of a defined testing scheme in one atmosphere, that is, 850°C / 30 MPa → 850°C / 60 MPa → 850°C / 80 MPa → 900°C / 30 MPa ..., which means that one specimen was tested under multiple thermal and mechanical load cycles at different temperatures in one atmosphere. This test scheme has proven successful as described in Ref. [32]. Some selected tests were additionally carried out with a separate specimen for one stress (80 MPa) at only two temperatures (1000°C and 1200°C) that verified the suitability of the test scheme.

The creep rate was determined from the slope in the secondary creep stage via linear regression fitting. Figure 1 shows a representative compressive creep deformation curve of BCZ20Y15 at 80 MPa and 1200°C.

Steady state creep in the secondary stage (simply termed "creep rate" hereafter) is usually thermally activated. The

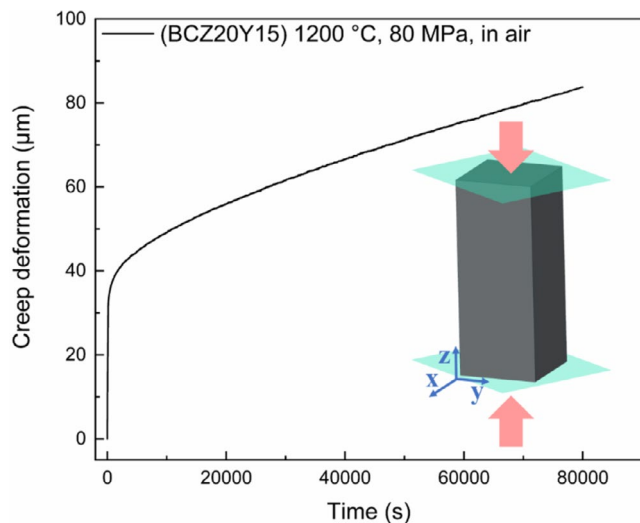


FIGURE 1 Representative creep deformation curve of BCZ20Y15 at a test temperature of 1200°C and an applied stress of 80 MPa in air [Color figure can be viewed at [wileyonlinelibrary.com](#)]

resulting creep rate $\dot{\epsilon}$ depends on the temperature T and the applied compressive stress σ , and can be described by the following equation^{27,32,33}:

$$\dot{\epsilon} = \dot{\epsilon}_0 \cdot A \cdot \left(\frac{\sigma}{\sigma_0} \right)^n \cdot \exp \left(-\frac{E_a}{RT} \right), \quad (1)$$

where A , n , E_a , and R are the stress-independent constant (Dorn constant), stress exponent, activation energy for creep and gas constant, respectively. $\dot{\epsilon}_0$ and σ_0 are 1 s^{-1} and 1 MPa , used for defining the dimensions of strain rate and stress.

The creep activation energy and stress exponent were obtained via global linear fitting of all results using the software “Origin.”

3 | RESULTS AND DISCUSSION

Figure 2 shows an Arrhenius plot of the creep rates of BCZ20Y15 vs. the reciprocal absolute temperature in the temperature range from 850°C to 1000°C in 4% H_2/Ar for stresses ranging from 30 to 80 MPa.

The temperature limit of the furnace in 4% H_2/Ar was 1000°C. Compared with the available phase diagrams of BaCeO_3 ³⁴ and BaZrO_3 ³⁵ for a rough estimation of BCZ20Y15's T_m (~2100 K), the applied temperatures are ~50% of the melting point, so it is reasonable that rather low creep rates were observed.

The creep activation energy was obtained via global linear fitting of all results using the software “Origin,” meaning that the fitting lines in Figure 2 share a same slope. In another word, 5 points together were linear fitted to get their shared slope, rather than 2 points and 3 points being linear fitted separately. The derived activation energy is ~160 kJ/

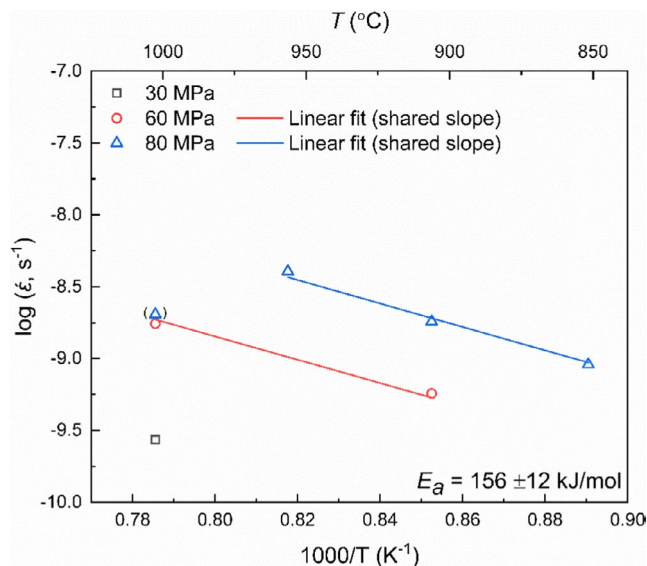


FIGURE 2 Arrhenius plot of the creep rates of BCZ20Y15 in 4% H_2/Ar for applied stresses ranging from 30 to 80 MPa as a function of the inverse temperature. The data point of 1000°C, 80 MPa (marked by the braces) was not included in the fit and the reasons will be discussed further down in the article [Color figure can be viewed at [wileyonlinelibrary.com](#)]

mol, indicating a rather weak temperature dependency for the temperature range of 850°C–1000°C. It should be noted that the 1000°C, 80 MPa data point was excluded from the activation energy calculation. This data point is associated with an unexpected behavior which will be discussed in more detail below. At the lowest applied compressive stress of 30 MPa, only at a temperature of 1000°C creep was observed. Thus, this isolated data point was not included in the global linear fitting. However, it can still be mathematically evaluated to check if it fits the global linear fitting results. Furthermore, the consistency between the mathematical description and the experimentally derived creep rates indicates the reliability of the results. However, for very low creep rates, thermal drift and noise may affect the reliability of the data.

Figure 3 shows the logarithmic plot of the creep rates of BCZ20Y15 as a function of applied stresses for temperatures ranging from 850°C–1000°C in 4% H_2/Ar .

Since global linear fitting was performed to analyze the slope, 4 points were analyzed together to get the slope rather than 2 groups of 2 points. The derived stress exponent is $n \approx 3$, which usually indicates a dislocation creep mechanism.³⁶ Such a mechanism commonly occurs in metals but has also been reported for ceramics.^{19,37} This mechanism has been observed in particular for ceramic membrane materials such as LSCF³⁸ and STF.²² The dislocation creep mechanism occurs typically under high stress and sufficiently high temperature enhancing the dislocation motion, which appears to be in agreement with the current testing conditions. The 850°C, 80 MPa and 950°C, 80 MPa data points can also

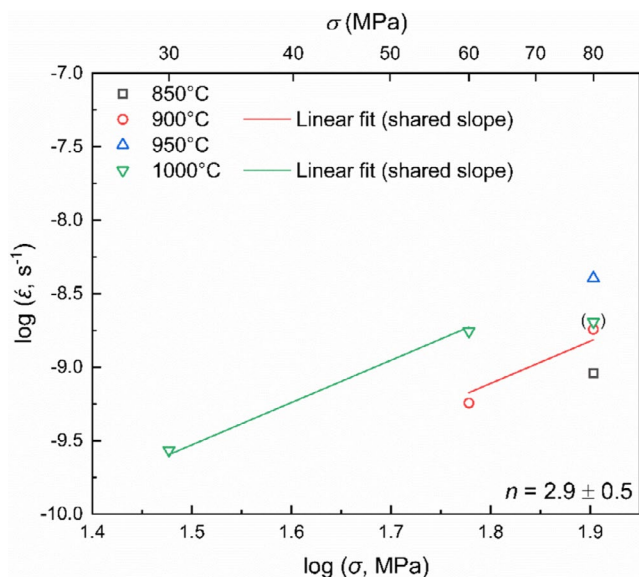


FIGURE 3 A double-logarithmic plot of the creep rates of BCZ20Y15 in 4% H₂/Ar as a function of applied compressive stresses for the temperature range of 850°C–1000°C. The data point of 1000°C, 80 MPa (marked by the braces) was not included in the fit and the reasons will be discussed further down in the article [Color figure can be viewed at wileyonlinelibrary.com]

be mathematically described by Equation 1, as mentioned above. Combined with the weak temperature dependency, the results from Figures 2 and 3 corroborate that the creep of BCZ20Y15 in 4% H₂/Ar, in the temperature and compressive stress ranges of 850°C–1000°C, 30 to 80 MPa, respectively, is governed by a dislocation creep mechanism. Note that, in case of a dislocation creep mechanism, the grain size will not influence the creep rate.³⁶

Figure 4 shows the microstructures of BCZ20Y15 before and after creep in a 4% H₂/Ar atmosphere.

For both, the 4% H₂/Ar post-creep tested specimen and the as-sintered reference specimen, the densities were ~98%. The grain sizes were also similar and in both cases ~20 μm, indicating that there was no pronounced grain growth or densification during the creep test. Therefore, the observed deformation during creep tests can be attributed completely to the creep deformation of BCZ20Y15.

XRD based investigations were performed for post-creep test specimens after being exposed to the test series under H₂/Ar and air. There was no indication of secondary phase formation within the limitation of the sensitivity of XRD. Hence, complementary detailed EDX characterizations in particular for post-creep specimens surface region was considered to be necessary. The respective results are shown in Figures 5 and 13. These EDX results also support the XRD results obtained in the current work, that is, only for the post-creep specimen, that was tested in air, a very thin decomposed layer in the proximity of the surface was observed.

For a detailed microstructural analysis, the material in the center of a specimen was characterized (Figure 5).

A clear grain boundary opening was observed (Figure 5B) at the location indicated in Figure 5A, similar as also reported in Ref. [24]. The gaping grain boundary is aligned with the direction of the compressive load applied, which was the longitudinal direction in Figure 5A, and agrees well with the observations in Ref. [24]. The stress tensor is complicated, but from a simplified stress model point of view, the specimen experienced compressive stress in the longitudinal direction (Z-direction) and tensile stress in transversal direction (Y-direction) in Figure 5A. The corresponding loading direction is marked by the white arrows on Figure 5B. EDX investigation was performed in the near surface region, since decomposition usually starts at the surface and then spreads deeper into the bulk of the specimen.³² As shown in Figure

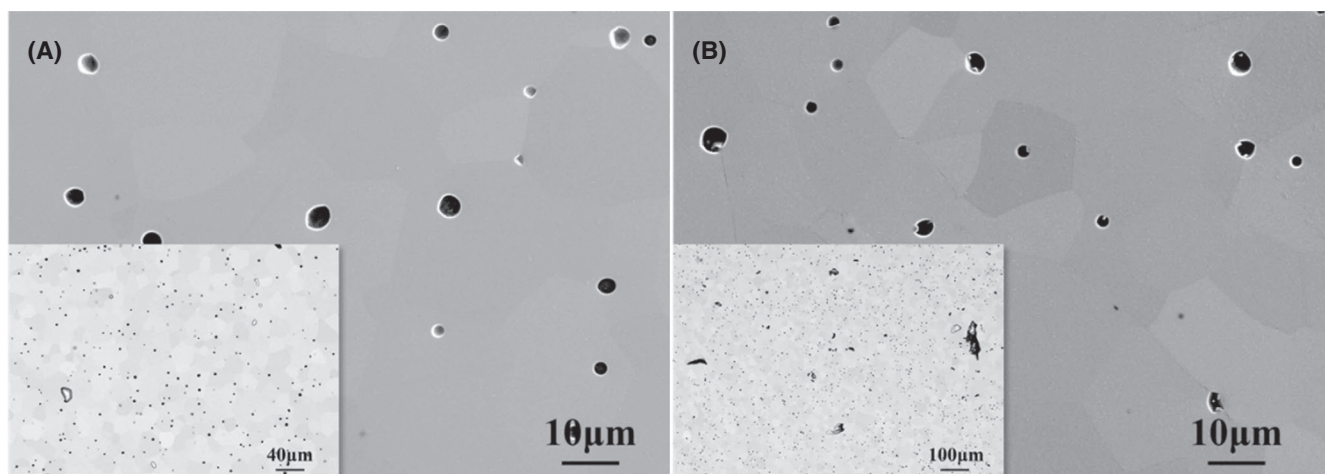


FIGURE 4 SEM micrographs of BCZ20Y15: (A) as-sintered specimen, and (B) specimen post-creep in 4% H₂/Ar. The insets show the polished sample surfaces at lower magnification, which were used for determining the density of the materials. The black spots on the polished surfaces are pores in the materials

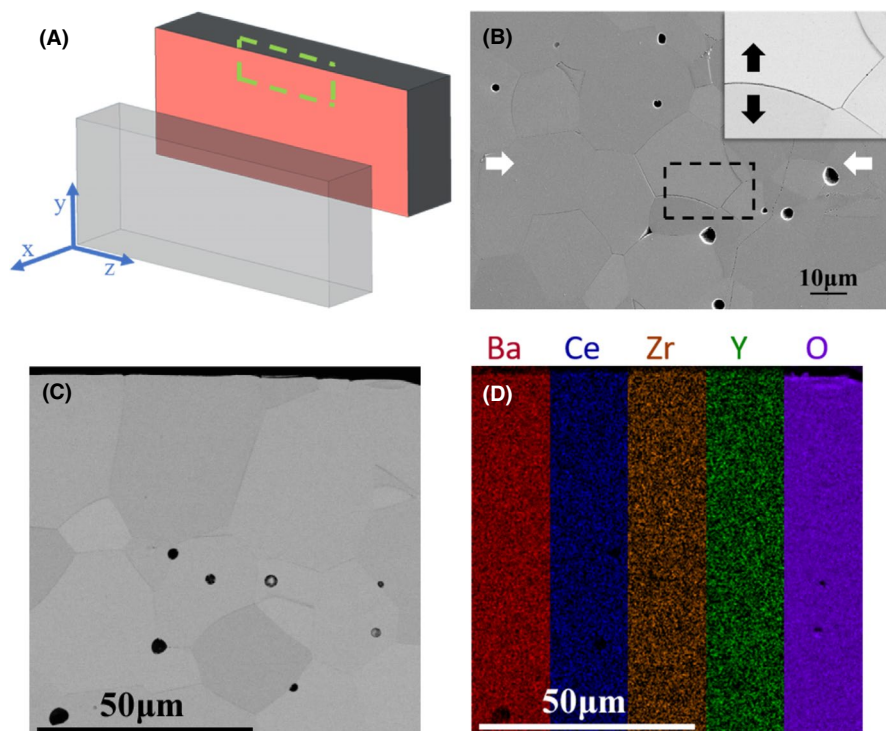


FIGURE 5 BCZ20Y15 was analyzed in more detail after creep in 4% H_2/Ar . (A) Schematic indicating the location in the sample, (B) SEM micrograph revealing grain boundary opening (marked by the black arrows) and loading direction (marked by the white arrows), (C) BSEM micrograph of a selected region which will be further analyzed via EDX in (D), (D) elemental analysis by EDX showing that all elements distribution homogeneous indicating no trace of decomposition [Color figure can be viewed at wileyonlinelibrary.com]

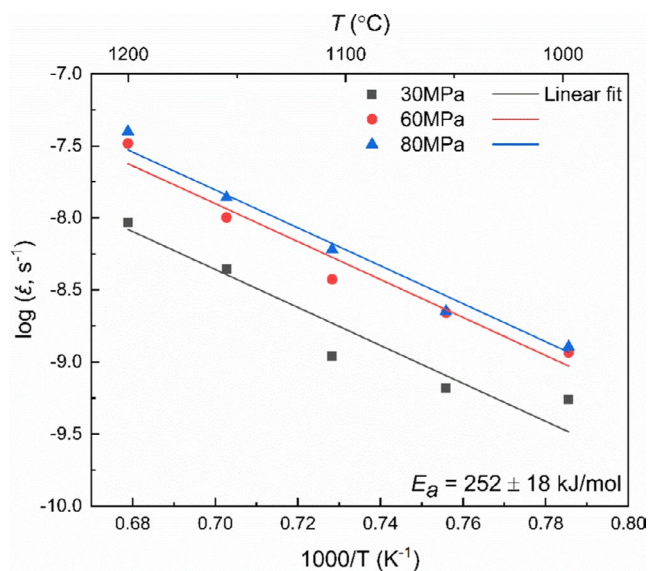


FIGURE 6 Arrhenius plot of the creep rates of BCZ20Y15 in air for applied compressive stresses ranging from 30 to 80 MPa as a function of inverse temperature. All data points at different stress levels over the temperature range of 1000°C–1200°C were included in the linear fit. Coefficient of determination (R^2) of the global linear fitting is ~ 0.96 [Color figure can be viewed at wileyonlinelibrary.com]

5C,D, comparison between topography and elemental mapping indicates that no noticeable decomposition.

Figure 6 shows an Arrhenius plot of the creep rates of BCZ20Y15 vs, reciprocal absolute temperature from 1000°C to 1200°C in air for stresses of 30, 60, and 80 MPa.

Since the creep tests in air were performed at higher temperatures, that is, at $\sim 70\%$ of the melting point of

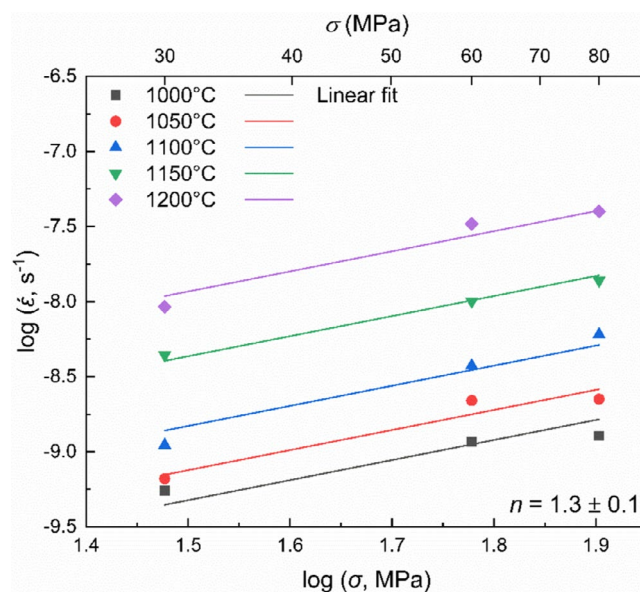


FIGURE 7 Double-logarithmic plot of the creep rates of BCZ20Y15 in air as function of the applied compressive stresses in the temperature range of 1000°C–1200°C [Color figure can be viewed at wileyonlinelibrary.com]

BCZ20Y15,^{34,35} higher creep rates are expected compared to the 4% H_2/Ar case, as indeed observed in Figure 6. The derived activation energy is ~ 250 kJ/mol, which is significantly higher than the derived activation energy in the 4% H_2/Ar case (Figure 2), revealing a stronger temperature dependency.

Figure 7 shows the logarithmic plot of the creep rates of BCZ20Y15 as a function of applied stresses for the temperature ranging from 1000°C–1200°C in air.

The derived stress exponent for the creep tests in air is ~ 1 , which is usually associated with a diffusional creep mechanism.³⁶ In the case of diffusional creep, the creep rate depends on the diffusivity of the slowest ion moving along the shortest diffusion path.^{38,39} This mechanism typically occurs at very high temperature and relatively low applied stresses. While based on the data presented in Figure 6, diffusional creep might be predominant in the temperature and stress range. Upon closer inspection of Figure 6, a division into two regimes can be suggested, as shown in Figure 8.

The higher temperature region and lower temperature region have different slopes in the Arrhenius plot and thus the corresponding activation energies are significantly different, that is ~ 350 and ~ 130 kJ/mol, respectively.

The activation energy determined for the low T regime is close to the activation energy determined in the creep tests under 4% H_2/Ar atmosphere (Figure 2), also indicating a weak temperature dependency. Further analysis of the stress exponent also indicates that the creep mechanism in the high T and low T regimes might be different, as shown in Figure 9.

The stress exponent n is ~ 1 for the lower temperature regime. Combined with the corresponding activation energy, the temperature dependency appears to be weak in this regime and as does the load dependency. Therefore, in the regime of $\sim 1050^\circ\text{C}$ and 1100°C , the predominant creep mechanism might

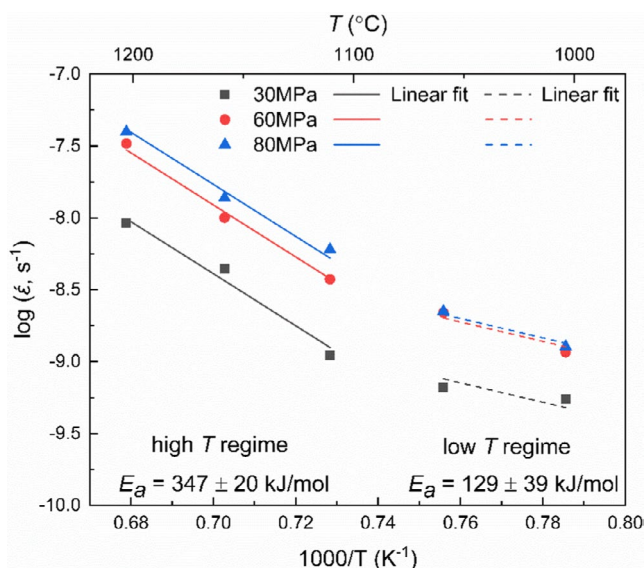


FIGURE 8 Arrhenius plot divided into a higher T and lower T regions according to the slopes of the creep rates of BCZ20Y15 in air for applied stress from 30 to 80 MPa as a function of inverse temperature. It should be noted that global linear fitting was performed to analyze the slopes, 6 points in low T range being analyzed together to get their shared slope. This is where the errors of straight lines fitting coming from, especially in low T regime. Coefficient of determination (R^2) of high T regime fitting and low T regime fitting are ~ 0.99 and ~ 0.97 , respectively. [Color figure can be viewed at [wileyonlinelibrary.com](#)]

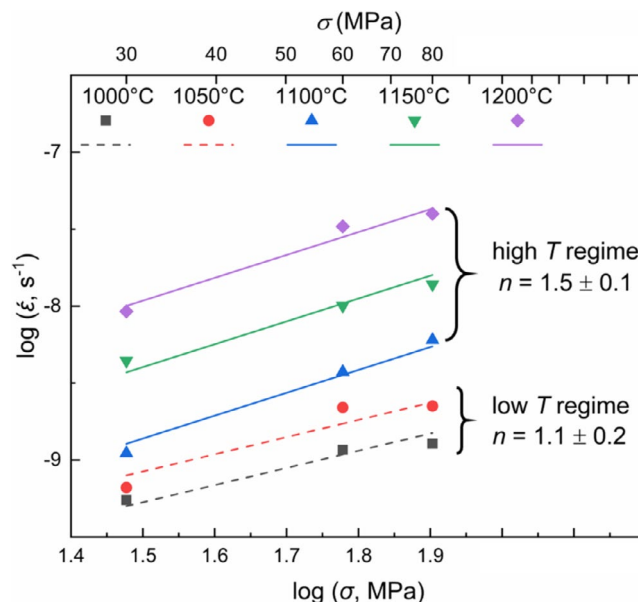


FIGURE 9 The double-logarithmic plot of the creep rate of BCZ20Y15 in air vs. applied compressive stress indicates a sub division into a high T and low T regime, that is $\geq 1100^\circ\text{C}$ and $\leq 1050^\circ\text{C}$, according to the slopes of the creep rates [Color figure can be viewed at [wileyonlinelibrary.com](#)]

change. As discussed above, the temperature range from 850°C to 1000°C is associated with a dislocation creep mechanism, while diffusional creep determines the behavior at temperatures $\geq 1100^\circ\text{C}$. It is therefore reasonable to assume that a transition regime exists, in which two mechanisms occur simultaneously. The presentation of the data in Figure 10 supports our assumption as further discussed below. In Figure 10, the creep behavior of BCZ20Y15 in air and in 4% H_2/Ar (indicated by full and open symbols, respectively) at $\sim 1000^\circ\text{C}$ is shown.

In both atmospheres, the creep rates at 80 and 60 MPa are almost equal and distinctly higher than at 30 MPa (data points inside the box in Figure 10A). In other words, at 1000°C the creep behaviors under different atmospheres are almost identical. From the double-logarithmic plot, it can be observed that for the 4% H_2/Ar case, at 1000°C , the load dependency becomes weak when the applied stress is higher than 60 MPa, indicating that the data point of 80 MPa belongs to a regime where two mechanisms exist simultaneously. This provides additional evidence for the change of the creep mechanism and supports our decision to exclude the creep data at 1000°C , 80 MPa, in 4% H_2/Ar , from the analysis in Figure 2. While the creep rate at 1000°C , 30 MPa is rather low, and therefore more affected by noise and thermal drift, the parallel lines shown in Figure 3 confirm the reliability of the analysis.

Figure 11 combines the data shown in Figures 2 and 8, presenting the creep behavior of BCZ20Y15 for the temperature range from 850°C to 1200°C , tested under applied compressive stresses ranging from 30 to 80 MPa, in both 4% H_2/Ar atmosphere and in air.

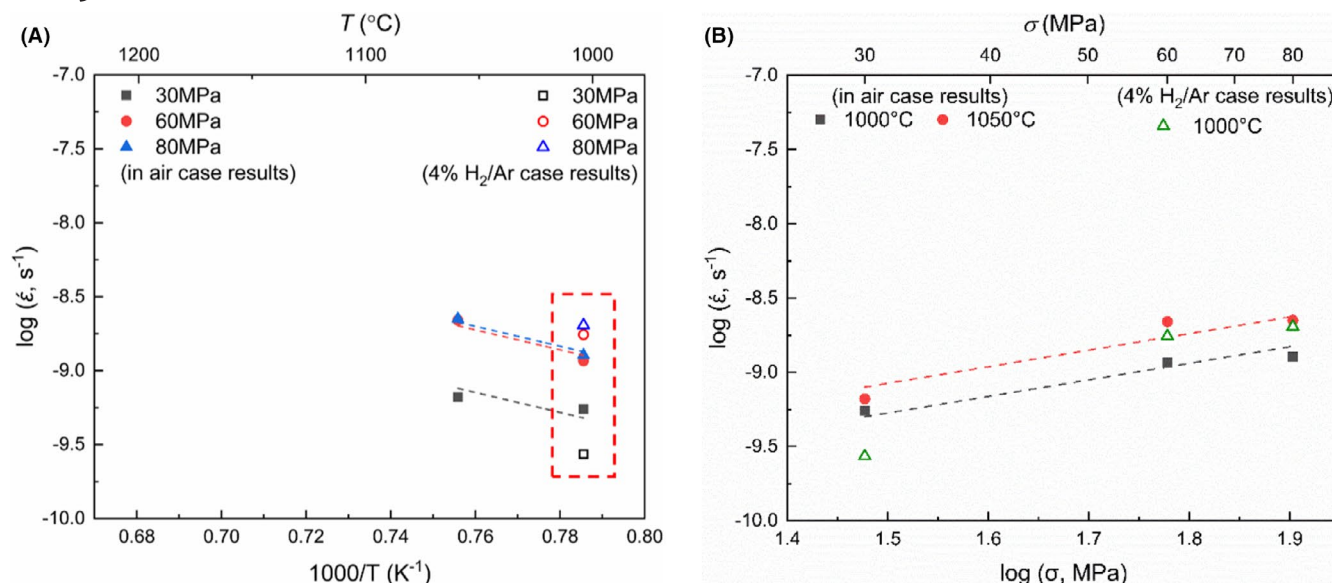


FIGURE 10 Combination and comparison of BCZ20Y15's creep behavior of both in air case results and in 4% H_2/Ar case results at $\sim 1000^\circ\text{C}$ to reveal the transition regime of the predominant creep mechanism. (A) Arrhenius plot, (B) double-logarithmic plot. The red dash line box marked data reveals an identical relatively high/low relationship of creep behavior in different atmospheres [Color figure can be viewed at wileyonlinelibrary.com]

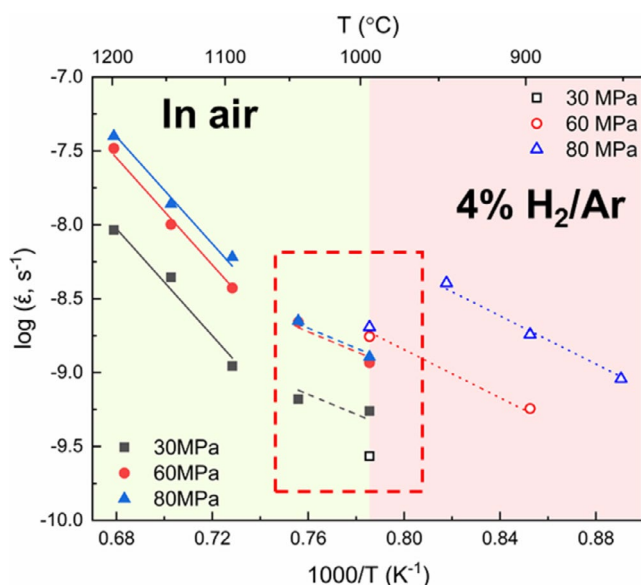


FIGURE 11 Arrhenius plot of the creep rates of BCZ20Y15 vs. the reciprocal absolute temperature in both 4% H_2/Ar atmosphere and air, for the temperature range of 850°C – 1200°C , under compressive applied stress ranging from 30 to 80 MPa. The red frame marked data indicates the transition regime of predominant creep mechanism, as also shown in Figure 10A [Color figure can be viewed at wileyonlinelibrary.com]

Different regimes can be distinguished in Figure 11. At temperatures lower than $\sim 1000^\circ\text{C}$, in 4% H_2/Ar , dislocation creep mechanism is the predominant mechanism, while at temperatures higher than $\sim 1100^\circ\text{C}$, in air, a regime associated with diffusional creep is observed. At intermediate temperatures ($\sim 1000^\circ\text{C}$, marked by the red frame), irrespective of the

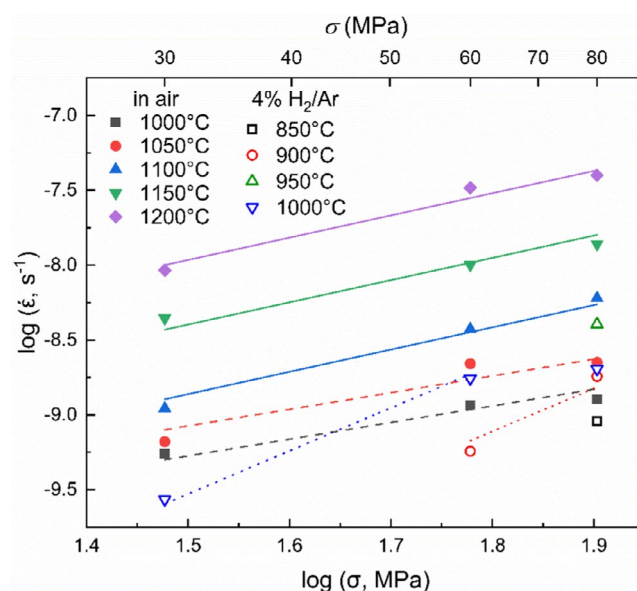


FIGURE 12 Double-logarithmic plot of the creep rate of BCZ20Y15 vs. the applied compressive stress in both 4% H_2/Ar atmosphere and in air, at temperatures ranging from 850°C to 1200°C [Color figure can be viewed at wileyonlinelibrary.com]

atmosphere, a shift in creep mechanism can be observed, as shown in Figure 12.

The three different slopes can be clearly observed in Figure 12, which is consistent with the three temperature regimes indicating different creep mechanisms in Figure 11.

The compressive creep behavior in Ar of a similar material, $\text{BaCe}_{0.8}\text{Y}_{0.2}\text{O}_{3-\alpha}$ (BCY20), at temperatures from 1200°C to 1450°C indicated a diffusional creep mechanism with a stress exponent of 1.1 ± 0.1 and an activation energy of

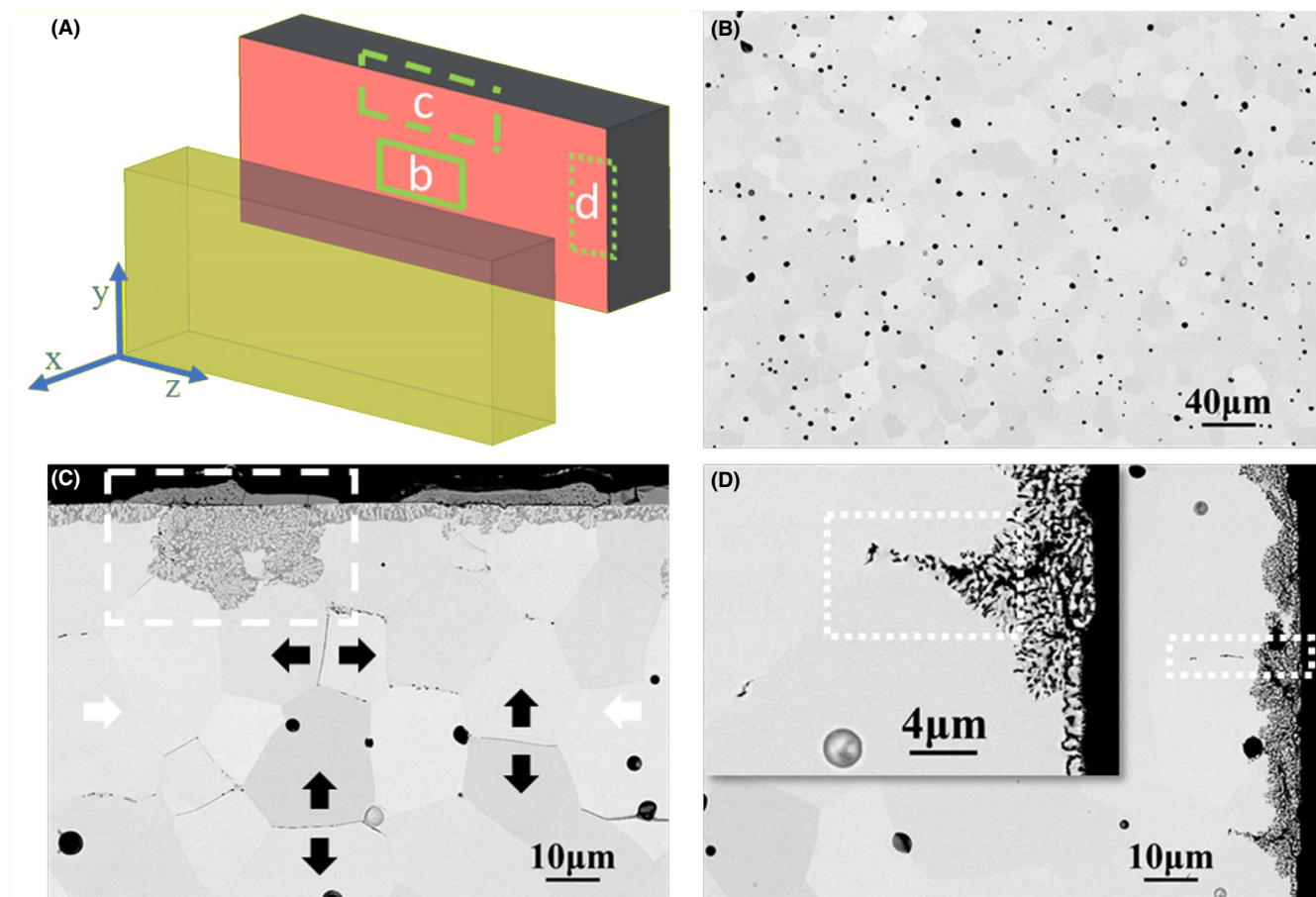


FIGURE 13 Microstructural observations after creep in air. (A) schematic of the location of the microstructural investigation on the polished post-creep specimen, (B) SEM micrograph of the central region showing porosity and grain structure, and (C, D) SEM micrographs of the near surface regions demonstrating the opening of the grain boundaries (marked by the black arrows; the white arrows indicate the loading direction) and material decomposition [Color figure can be viewed at wileyonlinelibrary.com]

343 ± 30 kJ/mol.³⁹ These results are in good agreement with our findings regarding the creep behavior in air in the temperature range from 1100°C to 1200°C. The activation energy values are comparable, in particular when the error bars are taken into account.

Figure 13 presents the microstructural observation of the post-creep specimen for the air case.

The density and grain size of the specimen after creep in air are ~98% and ~20 μm, respectively, and the same as determined for the as-sintered specimen Figure 4A. Hence, no indication of grain growth or densification during the creep test was observed and the deformation can be associated purely with the creep behavior. Moreover since the grain size of the material in this work is significantly larger than the grain size (~9 μm) of BCY20 studied in Ref. [39], that is ~20 μm vs. ~9 μm, also the grain size exponent was considered for a comparison of the creep rates, as shown in Equation 2.²⁰

$$\dot{\epsilon} = \dot{\epsilon}_0 \cdot A \cdot \left(\frac{d}{d_0}\right)^{-m} \cdot \left(\frac{\sigma}{\sigma_0}\right)^n \cdot \exp\left(-\frac{E_a}{RT}\right), \quad (2)$$

where d is the grain size and m the inverse grain size exponent, which has typically a value of 2 to 3 for a diffusional creep mechanism.¹⁹

The creep rate of BCY20 in Ref. [39] is $\sim 10^{-6}$ /s at 1200°C under a compressive stress of ~80 MPa, as estimated from the data presented. Thus, the creep rate reported is two orders of magnitude higher compared to $\sim 10^{-8}$ /s obtained in our work for the same stress/temperature combination. The distinct difference can be partially explained by the grain size, since the grain size of the material studied in this work is ~2 to 3 times larger than the one in Ref. [39]. Considering Equation 2, it is therefore reasonable that the creep rate obtained in this work is some orders of magnitude lower than reported in Ref. [39].

In addition to the grain size, differences in density might also contribute to the observed difference in the creep rates. The density of the BCY20³⁹ appears lower (~90%) than the density of our material which has a density of ~98%, when comparing the image analysis results of the SEM micrographs. Under identical test conditions, the specimen with higher porosity will likely exhibit a higher creep rate as discussed in detail on the basis of the Minimum Solid Area

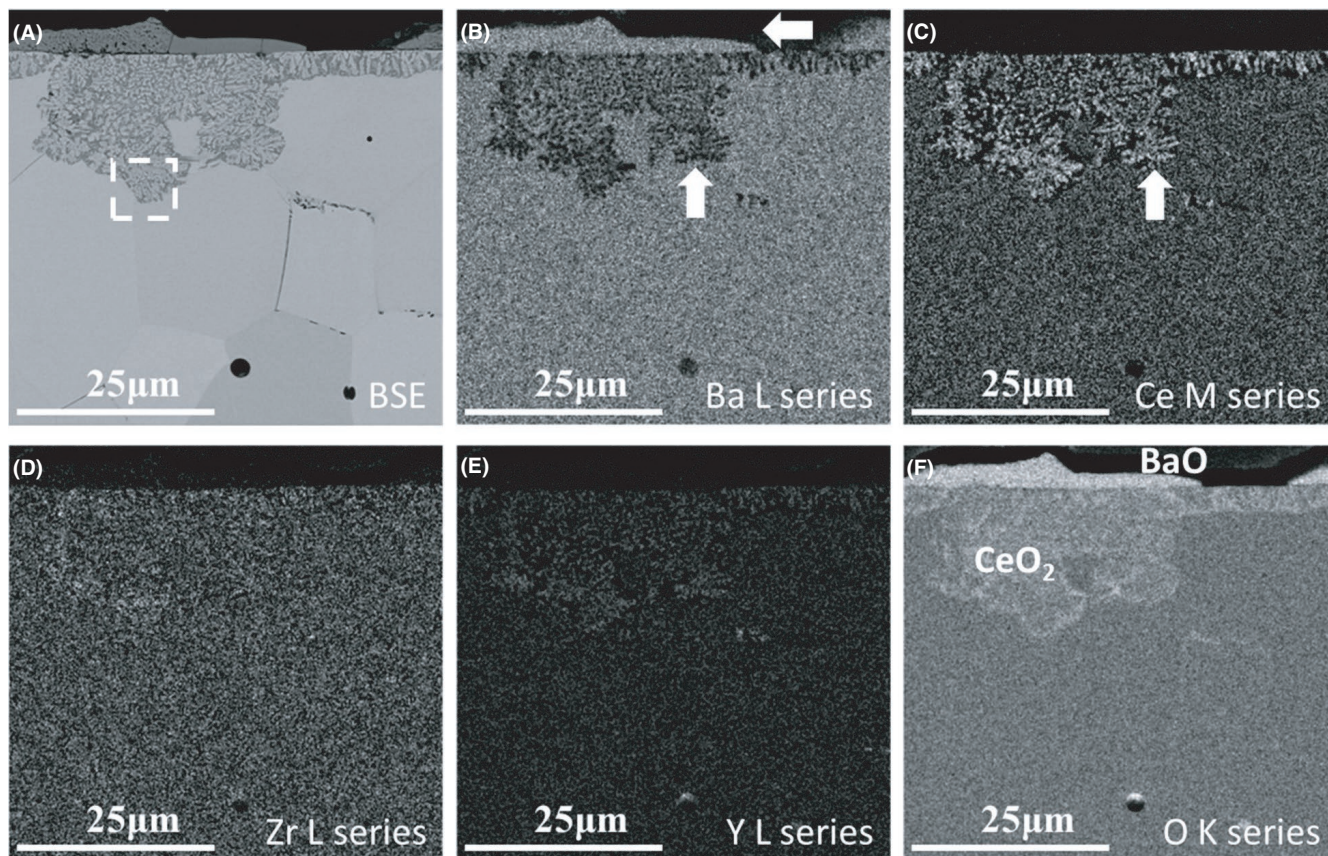


FIGURE 14 EDX element mapping of the degradation region on the post-creep in air specimen showing (A) the SEM micrograph indicating the decomposition spreading deeper following the grain boundary, and elemental distributions of (B) Ba (indicating Ba migration, as marked by the arrows, from dark contrast region to surface bright contrast region), (C) Ce (indicating Ce enrichment in the decomposition region, marked by arrow), (D) Zr (distributed homogeneously), (E) Y (showing slight compositional changes), (F) O (which indicates three different O levels in the region, i.e. the presence of additional two different phases with different O content)

(MSA) concept in Ref. [40,41]. Moreover the difference between creep rates for different porosities tend to become larger with increasing temperature.²⁴

As shown in Figure 13C, grain boundary opening can be clearly observed in the near-surface region (region c, marked in Figure 13A), while the grain boundaries appeared to be intact in the central bulk region (region b in Figure 13A) and close to the edge (region d in Figure 13A) as can be seen in Figure 13B,D. The differences regarding microstructural changes are likely related to the different stress states in the three locations. The central bulk region shows no decomposition, as can be seen, but in both near-surface regions (Figure 13C,D), the decomposition can be clearly seen.

In the region marked in Figure 13D, both decomposition and grain boundary opening can be observed. The decomposition spreads into the specimen starting from the surface and is enhanced by the presence of the grain boundaries. The opening of the grain boundaries might accelerate the decomposition, since oxygen can more easily reach sample regions located in the bulk. While based on Figure 13D, the decomposition might in turn also enhance the grain boundary

opening, a more detailed investigation of the process would be needed to describe the synergistic interplay of decomposition and grain boundary opening.

After the creep test in 4% H₂/Ar atmosphere over the temperature range of 850°C–1000°C, no decomposition was observed, while it had clearly occurred after creep in air at 1000°C–1200°C. Apparently, the combination of temperature and oxygen partial pressure has a distinct effect on the decomposition behavior of the material. For BCY20, which was tested in Ar atmosphere at 1200°C–1450°C,³⁹ no decomposition was reported. Oxygen partial pressure might, thus, be responsible for the decomposition rather than temperature, since no enhanced decomposition was observed at higher temperature in Ref. [39].

Figure 14 shows a detailed elemental analysis of the degradation zone observed in our work.

The decomposition zone appears to propagate along the grain boundary, as shown in Figure 14A, marked by the frame, which is consistent with the micrographs in Figure 13D. EDX elemental mappings show contrast variations in the different regions indicating local differences in the elemental composition. The loss of Ba underneath the surface

and the migration to the specimen surface can be clearly observed in Figure 14B. In the region of Ba loss, Ce enrichment has occurred, as shown in Figure 14C. Zr is distributed homogeneously exhibiting high stability against the decomposition, which is consistent with previous findings that Zr has high stability against chemical and thermal erosion,^{1-3,11,13,15} while some local redistribution of Y can be noticed (Figure 14D,E). Figure 14F shows the distribution of O; combining Figure 14F with B and C, it is shown that the decomposition of the sample leads to the formation of BaO and CeO₂. Based on the above analysis, it can be concluded that the decomposition observed after creep in air at temperatures from 1000°C to 1200°C is induced by the oxygen partial pressure, as also reported for the degradation of, for example, Cr₂AlC.³²

4 | CONCLUSIONS

In this work, the elevated temperature compressive creep behavior of BCZ20Y15 in different atmospheres was studied. From 850°C to 1000°C, in 4% H₂/Ar atmosphere, the stress exponent is ~3 and the activation energy ~160 kJ/mol, indicating a dislocation creep mechanism. For creep in the temperature range 1100°C–1200°C, in air, the stress exponent is ~1 and the activation energy ~350 kJ/mol, corresponding to a diffusional creep mechanism. At ~1000°C, a change of the predominant creep mechanism is observed in air. Grain growth and densification during the creep tests can be ruled out, which indicates that the observed deformation represents solely the creep behavior. After the creep tests in both atmospheres, gaping grain boundaries were observed near the surfaces, while decomposition was only observed for the specimen that was tested in air. The oxygen partial pressure is responsible for the observed decomposition rather than the temperature, which is important for the technical application, since as a material candidate for H₂ permeation, BCZ20Y15 will not be exposed to oxygen under realistic working conditions.

The observed creep rate of BCZ20Y15 in 4% H₂/Ar at 850°C is somewhat higher than the suggested critical compressive creep rate for commercial use of the membrane materials (1% per year). However, since the application temperature (~600°C–800°C) is lower than the test temperature, a rough extrapolation of the creep rate of BCZ20Y15 to the application temperature can be made, which results in a creep rate close to the envisaged 1% per year. Therefore, for the design of reliable membrane components, the thermomechanical stability and in particular the creep behavior needs to be considered.

ACKNOWLEDGEMENTS

This work was supported by the China Scholarship Council (CSC). The authors thank Dr. E. Wessel and Dr. D. Grüner

for the microstructural characterization and Mr. M. Turiaux for technical support.

ORCID

Wenyu Zhou  <https://orcid.org/0000-0003-3813-0217>

Olivier Guillon  <https://orcid.org/0000-0003-4831-5725>

REFERENCES

- Katahira K, Kohchi Y, Shimura T, Iwahara H. Protonic conduction in Zr-substituted BaCeO₃. *Solid State Ionics*. 2000;138(1–2):91–8.
- Ma X, Dai J, Zhang H, Reisner DE. Protonic conductivity nanostructured ceramic film with improved resistance to carbon dioxide at elevated temperatures. *Surf Coat Technol*. 2005;200(5–6):1252–8.
- Sawant P, Varma S, Wani B, Bharadwaj S. Synthesis, stability and conductivity of BaCe_{0.8-x}Zr_xY_{0.2}O_{3-δ} as electrolyte for proton conducting SOFC. *Int J Hydrogen Energy*. 2012;37(4):3848–56.
- Yano M, Tomita A, Sano M, Hibino T. Recent advances in single-chamber solid oxide fuel cells: a review. *Solid State Ionics*. 2007;177(39–40):3351–9.
- Radenahmad N, Afif A, Petra PI, Rahman SM, Eriksson S-G, Azad AK. Proton-conducting electrolytes for direct methanol and direct urea fuel cells—A state-of-the-art review. *Renew Sustain Energy Rev*. 2016;57:1347–58.
- Kreuer K. Proton-conducting oxides. *Annu Rev Mater Res*. 2003;33(1):333–59.
- Phair J, Badwal S. Review of proton conductors for hydrogen separation. *Ionics*. 2006;12(2):103–15.
- Barison S, Battagliarin M, Cavallin T, Daolio S, Doubova L, Fabrizio M, et al. Barium non-stoichiometry role on the properties of Ba_{1+x}Ce_{0.65}Zr_{0.20}Y_{0.15}O_{3-δ} proton conductors for IT-SOFCs. *Fuel Cells*. 2008;8(5):360–8.
- Li J, Luo J-L, Chuang KT, Sanger AR. Chemical stability of Y-doped Ba (Ce, Zr) O₃ perovskites in H₂S-containing H₂. *Electrochim Acta*. 2008;53(10):3701–7.
- Lv J, Wang L, Lei D, Guo H, Kumar R. Sintering, chemical stability and electrical conductivity of the perovskite proton conductors BaCe_{0.45}Zr_{0.45}M_{0.1}O_{3-δ} (M= In, Y, Gd, Sm). *J Alloys Compounds*. 2009;467(1–2):376–82.
- Yoo Y, Lim N. Performance and stability of proton conducting solid oxide fuel cells based on yttrium-doped barium cerate-zirconate thin-film electrolyte. *J Power Sources*. 2013;229:48–57.
- Zhong Z. Stability and conductivity study of the BaCe_{0.9-x}Zr_xY_{0.1}O_{2.95} systems. *Solid State Ionics*. 2007;178(3–4):213–20.
- Mortalò C, Rebollo E, Escolástico S, Deambrosis S, Haas-Santo K, Rancan M, et al. Enhanced sulfur tolerance of BaCe_{0.65}Zr_{0.20}Y_{0.15}O_{3-δ}-Ce_{0.85}Gd_{0.15}O_{2-δ} composite for hydrogen separation membranes. *J Membrane Sci*. 2018;564:123–32.
- Rebollo E, Mortalo C, Escolástico S, Boldrini S, Barison S, Serra JM, et al. Exceptional hydrogen permeation of all-ceramic composite robust membranes based on BaCe_{0.65}Zr_{0.20}Y_{0.15}O_{3-δ} and Y- or Gd-doped ceria. *Energy Environ Sci*. 2015;8(12):3675–86.
- Barison S, Battagliarin M, Cavallin T, Doubova L, Fabrizio M, Mortalo C, et al. High conductivity and chemical stability of BaCe_{1-x-y}Zr_xY_yO_{3-δ} proton conductors prepared by a sol-gel method. *J Mater Chem*. 2008;18(42):5120–8.
- Doubova L, Barison S, Boldrini S, Fabrizio M, Mortalo C, Pagura C. Conductivity studies of sol-gel prepared BaCe_{0.85-x}Zr_xY_{0.15}O_{3-δ}

- solid electrolytes using impedance spectroscopy. *J Appl Electrochem*. 2009;39(11):2129–41.
17. Deibert W, Ivanova ME, Baumann S, Guillon O, Meulenberg WA. Ion-conducting ceramic membrane reactors for high-temperature applications. *J Membr Sci*. 2017;543:79–97.
 18. Meulenberg WA, Schulze-Küppers F, Deibert W, Gestel TV, Baumann S. Ceramic membranes: materials—components—potential applications. *ChemBioEng Rev*. 2019;6(6):198–208.
 19. Pelleg J. Creep in ceramics, Creep in Ceramics, Springer. 2017;41–61.
 20. Yi J, Lein H, Grande T, Yakovlev S, Bouwmeester H. High-temperature compressive creep behaviour of the perovskite-type oxide $\text{Ba}_{0.5}\text{Sr}_{0.5}\text{Co}_{0.8}\text{Fe}_{0.2}\text{O}_{3-\delta}$. *Solid State Ionics*. 2009;180(36–39):1564–8.
 21. Radovic M, Barsoum M, El-Raghy T, Wiederhorn S. Tensile creep of fine grained (3–5 μm) Ti_3SiC_2 in the 1000–1200°C temperature range. *Acta Mater*. 2001;49(19):4103–12.
 22. Ten Donkelaar S, Stournari V, Malzbender J, Nijmeijer A, Bouwmeester HJ. High-temperature compressive creep behaviour of perovskite-type oxides $\text{SrTi}_{1-x}\text{Fe}_x\text{O}_{3-\delta}$. *J Eur Ceram Soc*. 2015;35(15):4203–9.
 23. Wei J, Malzbender J. Steady state creep of Ni-8YSZ substrates for application in solid oxide fuel and electrolysis cells. *J Power Sources*. 2017;360:1–10.
 24. Zou Y, Schulze-Küppers F, Balaguer M, Malzbender J, Krüger M. Creep behavior of porous $\text{La}_{0.6}\text{Sr}_{0.4}\text{Co}_{0.2}\text{Fe}_{0.8}\text{O}_{3-\delta}$ substrate material for oxygen separation application. *J Eur Ceram Soc*. 2018;38(4):1702–10.
 25. Zhou W, Malzbender J, Zeng F, Deibert W, Guillon O, Schwaiger R, et al. Mechanical properties of $\text{BaCe}_{0.65}\text{Zr}_{0.2}\text{Y}_{0.15}\text{O}_{3-\delta}$ proton-conducting material determined using different nanoindentation methods. *J Eur Ceram Soc*. 2020;40(15):5653–61. <https://doi.org/10.1016/j.jeurceramsoc.2020.07.044>
 26. Schneider CA, Rasband WS, Eliceiri KW. NIH Image to ImageJ: 25 years of image analysis. *Nat Methods*. 2012;9(7):671–5.
 27. Li X, Gonzalez-Julian J, Malzbender J. Fabrication and mechanical performance of Ti_2AlN prepared by FAST/SPS. *J Eur Ceram Soc*. 2020;40(13):4445–53.
 28. Deibert W, Stournari V, Ivanova ME, Escolástico S, Serra JM, Malzbender J, et al. Effect of microstructure on electrical and mechanical properties of $\text{La}_{5.4}\text{WO}_{12-\delta}$ proton conductor. *J Eur Ceram Soc*. 2018;38(10):3527–38.
 29. Zou Y, Schulze-Küppers F, Malzbender J. Creep behavior of porous $\text{La}_{0.6}\text{Sr}_{0.4}\text{Co}_{0.2}\text{Fe}_{0.8}\text{O}_{3-\delta}$ oxygen transport membrane supports. *Ceram Int*. 2015;41(3):4064–9.
 30. Rutkowski B, Malzbender J, Beck T, Steinbrech R, Singheiser L. Creep behaviour of tubular $\text{Ba}_{0.5}\text{Sr}_{0.5}\text{Co}_{0.8}\text{Fe}_{0.2}\text{O}_{3-\delta}$ gas separation membranes. *J Eur Ceram Soc*. 2011;31(4):493–9.
 31. Schulz M, Kriegel R, Burckhardt W. Modeling of oxygen flux and stress distribution for $\text{Ba}_{0.5}\text{Sr}_{0.5}\text{Co}_{0.8}\text{Fe}_{0.2}\text{O}_{3-\delta}$ membranes at application conditions. *Intern Conf Inorg Membranes, Jpn*; 2008.
 32. Araki W, Gonzalez-Julian J, Malzbender J. High temperature compressive creep of dense and porous Cr_2AlC in air. *J Eur Ceram Soc*. 2019;39(13):3660–7.
 33. Radovic M, Barsoum M, El-Raghy T, Wiederhorn S. Tensile creep of coarse-grained Ti_3SiC_2 in the 1000–1200°C temperature range. *J Alloy Compd*. 2003;361(1–2):299–312.
 34. https://phaseonline.ceramics.org/ped_figure_search. PED Fig. No. 5134 (the database was accessed on. 2019;10:12).
 35. https://phaseonline.ceramics.org/ped_figure_search. PED Fig. No. 14154 (the database was accessed on. 2019;10:12).
 36. Green DJ. An introduction to the mechanical properties of ceramics. Cambridge, UK: Cambridge University Press; 1998.
 37. Kassner ME. Fundamentals of creep in metals and alloys. Oxford, UK: Butterworth-Heinemann; 2015.
 38. Huang B, Steinbrech R, Baumann S, Malzbender J. Creep behavior and its correlation with defect chemistry of $\text{La}_{0.58}\text{Sr}_{0.4}\text{Co}_{0.2}\text{Fe}_{0.8}\text{O}_{3-\delta}$. *Acta Mater*. 2012;60(6–7):2479–84.
 39. Goretta K, Park E, Guan J, Balachandran U, Dorris S, Routbort J. Diffusional creep of $\text{BaCe}_{0.8}\text{Y}_{0.2}\text{O}_{3-\alpha}$ mixed conductors. *Solid State Ionics*. 1998;111(3–4):295–9.
 40. Rice R. Evaluation and extension of physical property-porosity models based on minimum solid area. *J Mater Sci*. 1996;31(1):102–18.
 41. Rice RW. Porosity of ceramics: Properties and applications. Boca Raton, FL: CRC Press; 1998.

How to cite this article: Zhou W, Malzbender J, Deibert W, et al. High temperature compressive creep behavior of $\text{BaCe}_{0.65}\text{Zr}_{0.2}\text{Y}_{0.15}\text{O}_{3-\delta}$ in air and 4% H_2/Ar . *J Am Ceram Soc*. 2021;104:2730–2740. <https://doi.org/10.1111/jace.17715>